Variable-Magnification Optical Stimulator for Training and Validation of Spaceborne Vision-Based Navigation

Connor Beierle* and Simone D'Amico†
Stanford University, Stanford, California 94305-4035

DOI: 10.2514/1.A34337

This paper addresses the design, calibration, and utilization of a hardware-in-the loop optical stimulator for the training and validation of vision-based sensors and algorithms used for spaceborne navigation. This testbed overcomes deficiencies of existing approaches in literature, which mainly focus on emulating single operational zones such as inertial, far-range, or close-range relative navigation. Consequently, the behavior of vision-based sensors and algorithms operating in mixed or transitioning navigation regimes have remained poorly assessed before launch. To address these issues, this novel optical stimulator reproduces the large geometric and radiometric dynamic range of the space environment with a pair of lenses to achieve variable magnification of an organic light emitting diode monitor. This approach is shown to support vision-based sensors of both narrow and wide field of view, increase the radiometric dynamic range of the testbed, and emulate close-range scenarios when light from an object is not collimated. A calibration procedure is presented that places sources of light at the intended angular location over the magnification range in the presence of varying distortions. The calibrated testbed is then used to simulate dynamic inertial and relative navigation scenarios of operational relevance. These hardware-in-the-loop simulations allow for the training and validation of optical hardware, software, and algorithms for future distributed space systems.

Nomenclature

A	=	area, m^2
a	=	semimajor axis, m
e	=	eccentricity
f	=	focal length, m
h	=	optical height, m
I	=	irradiance, $W \cdot m^{-2}$
i	=	inclination, deg
L	=	testbed length, m
M	=	magnification
m	=	visual magnitude
N	=	number of pixels
r	=	interspacecraft separation, m
s	=	optical separation, m
u	=	actuator stroke, m
Ω	=	solid angle, sr

I. Introduction

VISION-BASED sensors (VBSs) are a ubiquitous part of the satellite navigation system. Common sensors used for inertial navigation are star trackers and sun and Earth sensors. These sensors are also extensively used for spacecraft relative navigation and have been used in flight (or planned) to facilitate autonomous rendezvous [1–4], formation flying [5,6], swarm operations [7], near Earth object exploration [8,9], space situational awareness [10], space debris removal [11–13], lifetime prolongation through on-orbit servicing [14,15], and many more. Relative vision-based navigation techniques can be applied at interspacecraft separations ranging from hundreds of kilometers down to virtually zero separation in many orbit regimes. At large separation distances, the relative motion between spacecraft can be determined using angles-only navigation (AON), which has been considered in several research studies [16–20] and applied on orbit [3,21,22]. In this navigation mode, the observer spacecraft is attempting to estimate the relative orbital motion of a target space object using only optical bearing angles obtained by a VBS. At close range, pose estimation algorithms can be used to estimate relative position, velocity, attitude, and other parameters of a target space object from a single image. Close-range vision-based pose estimation algorithms can use known visual markers and/or computer-aided models of the space object to estimate the relative position and orientation [23–26].

Testing a VBS on the ground has become of increasing importance as autonomous, smaller, mass-produced satellites demand the ability to verify vision-based hardware and software reliably and more efficiently. Future missions with autonomous vehicles are increasing the range of operations and imposing demanding angular and radiometric sensor detection requirements on the vision–navigation payload. In addition, there is great interest in the engineering community in vision-based navigation systems capable of bridging the gap between far- and close-range navigation techniques. This gap comprises mixed navigation modes (i.e., performing inertial and far-range relative navigation simultaneously) as well as transitions between navigation modes (i.e., transition from far- to close-range relative navigation) and highly variable modes (i.e., optical navigation at highly varying separation and illumination conditions). For example, the long-range VBS used on the autonomous rendezvous demonstration using GPS and optical navigation experiment conducted in the framework of the PRISMA (OHB Sweden) mission suffered from blooming when the resident space object was in view, which impacts the quality of its inertial and relative navigation solution [3]. Before the next generation of vision-based navigation systems can be deployed in space, a high-fidelity, high-dynamic-range testbed is necessary to properly verify algorithms, software, and hardware in terms of functionality, performance, and robustness.

Spaceborne vision-based navigation testing facilities have historically been designed to calibrate and assess only star trackers [27–31]. Typically, a testbed consists of a static star field and a single corrective optic (CO) to account for the finite distance between the optical stimulator (OS) and VBS. These systems typically have limited geometrical imaging precision, radiometric dynamic range, and contrast ratio, and they lack the appropriate software to simulate stellar objects (SOs) and nonstellar objects (NSOs) in real time and closed loop.

Rufino and Moccia created a testing facility that consisted of a cathode ray tube monitor stimulating a star tracker through a CO [27]. The cathode ray tube testbed was enclosed in a $1.8 \times 0.6 \times 0.6$ m shroud with explicit calibration efforts invested to quantify the

Received 22 June 2018; revision received 13 November 2018; accepted for publication 21 December 2018; published online 6 February 2019.

*Doctoral Candidate, Department of Aeronautics and Astronautics, Space Rendezvous Laboratory, Durand Building, 496 Lomita Mall.

†Director, Space Rendezvous Laboratory, Department of Aeronautics and Astronautics, Durand Building, 496 Lomita Mall.

irradiance output of the monitor versus digital count. The methodology to simulate an SO was to illuminate a single pixel, which limited the geometrical resolution of the testbed to the instantaneous field of view (iFOV) of a monitor pixel ($\sim 50''$). The authors correct for distortions introduced by the CO in software, and quantify the temporal nature of a dynamic simulation rigorously. This testbed, however, did not simulate NSOs within the FOV.

The Jenoptik optical sky field simulator used by DLR, German Aerospace Center is a compact device that is attached to an arbitrary star tracker through a custom adapter [30]. A simulated scene stimulates a star tracker with collimated light and accounts for optical distortions by warping the intended scene as well. The distortion introduced by the CO is isolated from distortion due to VBS and is characterized using a pair of fourth-order calibration polynomials, which results in the ability to render a single star to within $\sim 10''$. Pixel intensity is commanded using a Gaussian point-spread function based off star visual magnitudes. This testbed has the ability to render planetary objects (sun, moon, asteroids) but does not describe the ability to simulate satellites within the sensor's field of view (FOV).

The Optical Stimulator System for VBS testbed created by the Technical University of Denmark (DTU) consists of a computer monitor viewed by a VBS through a CO [32]. The testbed is large and encased in a shroud, but no other mentions of radiometric emulation are described. Geometrically, the authors account for optical distortion by rendering a scene to the monitor, which is warped using openCV [33]. The resulting attitude solutions differ in the single arcsecond range from the intended attitude. The authors do not distinguish between distortion of the camera's optical elements and the distortion introduced by the CO. This testbed has the capability to simulate satellites as well.

The fixed monitor and single CO architecture used in the aforementioned testbeds has several fundamental limitations. First, this design is unable to support testing of both narrow and wide FOV VBSs. For researchers working with multiple VBSs of different FOV (i.e., short range cameras, horizon sensors, star trackers, telescopes, etc.), exchanging COs and recalibrating a testbed is a major inefficiency. Second, these testbeds are unable to emulate close-range scenarios when light from an object in the FOV is not collimated. Additional limitations of previous optical testbeds consist of insufficiencies in angular accuracy, radiometric dynamic range, the ability to simulate a rapidly changing scene, accounting for geometric distortion, matching radiometric characteristics, simulating multiple, and mixed and transition navigation modes (i.e., inertial, far-range, and close-range) simultaneously. With these limitations in mind, it is evident that advancements to a laboratory testing environment are necessary to rapidly verify the next generation of spaceborne vision-based navigation systems.

This introduction is followed by an establishment of functional and performance requirements presented in Sec. II intended to steer the testbed design process presented in Sec. III. Section IV describes the manner in which synthetic scenes are generated. A summary of the OS geometric and radiometric calibration is then presented in Sec. V. It will be demonstrated that a fully calibrated system is capable of positioning a point source of light to within $5''$ of angular accuracy over eight orders of radiometric magnitude. Section VI outlines results from two hardware-in-the-loop (HIL) experiments. The first HIL experiment simulates an AON scenario at far range, and the second HIL experiment simulates a pose estimation scenario at close range. Results are analyzed and discussed before the conclusions and way forward in Sec. VII.

II. Testbed Requirements

The objective of this testbed is to stimulate a broad range of space-capable VBSs using synthetically created scenes that are highly representative of the space environment. The scenes of interest consist of SOs and NSOs, which impose their own independent set of functional and performance requirements on the testbed.

A. Stellar Objects

From a functional standpoint, the OS should produce an image realistic enough for a star tracker to obtain a lock and produce an inertial attitude solution based off of observed SOs. This overall goal imposes requirements on the system's ability to geometrically place an SO and simulate its radiometric characteristics. If the aforementioned requirements are met, simulated SOs observed by a VBS can be identified within a star catalog. Ideally, the monitor for the OS should be able to simulate SOs within the angular resolution and detection limit of the VBS, which for considered cameras are 1–10" and a visual magnitude range of 2–7, respectively [34]. The relationship between visual magnitude and irradiance is given by

$$m = -2.5\log_{10}\left(\frac{I_{\text{so}}}{I_0}\right) \tag{1}$$

where m is the visual magnitude of a SO, I_0 is the reference irradiance of a visual magnitude 0 SO ($I_0 = 3.1 \times 10^{-9}$ W $\cdot$ m^{-2}), and I_{so} is the irradiance of an observed SO.

Using Eq. (1), the aforementioned visual magnitude bounds correspond to an irradiance range of $5 \times 10^{-12} \leq I_{\text{so}} \leq 5 \times 10^{-10}$ W $\cdot$ m^{-2}. The radiometric performance requirement associated with simulating an SO imposed on the OS is to be able to radiate light over this irradiance range.

B. Nonstellar Objects

An NSO is defined to be a space object that is not a star. Illumination of the NSO by natural or artificial sources will reflect off the object and, if unobstructed, arrive at an observing VBS. The model used to quantify the irradiance received by an observing VBS is given by

$$I_{\text{nso}} = a\left(\frac{\Omega}{2\pi}\right)I_{\text{solar}} = a\left(\frac{A}{2\pi r^2}\right)I_{\text{solar}} \tag{2}$$

where I_{nso} is the irradiance emitted by the NSO; a is the reflectance coefficient of the NSO; Ω is the solid angle subtended by the NSO; A is the characteristic area of the NSO; r is the interobject separation; and I_{solar} is the visible solar irradiance of 620 W $\cdot$ m^{-2} at 1 astronomical unit. Note that the characteristic area of the NSO is functionally dependent on its attitude and position relative to an observer.

The NSO radiometric performance requirements imposed on the OS monitor are not only a function of characteristics of the simulated NSO (i.e., range of r, A, a) but also on the instantaneous field of view (iFOV) of the OS monitor pixels, $i\text{FOV}_{\text{os}}$. The number of OS monitor pixels (N) required to match this geometry is calculated using similar triangles and is given by

$$N = \frac{\sqrt{\Omega}}{i\text{FOV}_{\text{os}}} \tag{3}$$

The irradiance which must be emitted by a single OS monitor pixel (I_{os}) is taken to be

$$I_{\text{os}} = \frac{I_{\text{nso}}}{N^2} \tag{4}$$

Equation (4) is used to compute the NSO irradiance performance requirement imposed on an OS monitor pixel. For example, consider an NSO with $A = 2500$ cm^2, $a = 1 \times 10^{-3}$, over an interobject separation ranging from 10 m to 100 km, and $i\text{FOV}_{\text{os}} = 10''$. The NSO irradiance, subtended solid angle, and number of monitor pixels over a range of interobject separation are tabulated in Table 1.

These quantities are used with Eq. (4) to compute an NSO peak irradiance performance requirement imposed on a single OS monitor pixel of $I_{\text{os}} = 2.5 \times 10^{-10}$ W $\cdot$ m^{-2}.

C. Monitor Irradiance

Table 2 summarizes the lower and upper irradiance bounds required to simulate an SO and NSO posed by future autonomous rendezvous missions [1,5,14].

The monitor's dynamic range should be as large as possible to accurately simulate dim SOs and bright NSOs at close proximity.

Table 1 NSO solid angle and irradiance for a given interobject separation (these quantities are used with a known $i\text{FOV}_{os}$ to compute the number of pixels required to match NSO irradiance)

r, m	$\sqrt{\Omega}$, deg	I_{nso}, W · m^2	N, pixels
1×10^5	5×10^{-6}	2.5×10^{-12}	1×10^{-1}
1×10^4	5×10^{-5}	2.5×10^{-10}	1×10^{0}
1×10^3	5×10^{-4}	2.5×10^{-8}	1×10^{1}
1×10^2	5×10^{-3}	2.5×10^{-6}	1×10^{2}
1×10^1	5×10^{-2}	2.5×10^{-4}	1×10^{3}

Table 2 Irradiance requirements to simulate an SO and NSO

Object	Minimum irradiance, W · m^{-2}	Maximum irradiance, W · m^{-2}
SO	$5 \cdot 10^{-12}$	$5 \cdot 10^{-10}$
NSO	$2 \cdot 10^{-11}$	$2 \cdot 10^{-04}$

A market survey identified that most commercial-off-the-shelf monitors have individual pixels that span 2–3 orders of radiometric magnitude. By allocating a large number of adjacent monitor pixels, the radiometric output of the monitor can span several orders of magnitude. For example, a monitor with 2×10^6 pixels and single pixel irradiance of 10^{-8} W · m^{-2} is capable of matching irradiance levels up to 2×10^{-2} W · m^{-2}. By selecting a monitor with over 2×10^6 pixels and a individual pixel dynamic range of 10^{-11} through 10^{-8} W · m^{-2}, all SOs and NSOs of interest (with respect to the testbed requirements) can be simulated.

III. Design of Optical Stimulator

The OS design under consideration consists of two lenses and a monitor. By moving the two lenses and monitor relative to each other, variable magnification of the monitor can be achieved to enable highly dynamic emulation of the space environment. The dual-lens configuration is depicted in Fig. 1.

In Fig. 1, h_m is the vertical height of the monitor; h_{i1} and h_{i2} are the vertical heights of the real and virtual images, respectively; s_{o1} is the separation between the monitor and lens 1; s_{o2} is the separation between lens 2 and the real image; s_{i1} is the separation between lens 1 and the real image; and s_{i2} is the separation between lens 2 and the virtual image. By moving the monitor, lens 1, and lens 2 relative to each other, variable magnification of the monitor can be achieved. The magnification M of the monitor produced by the first lens is given by

$$M = -\frac{s_{i1}}{s_{o1}} \tag{5}$$

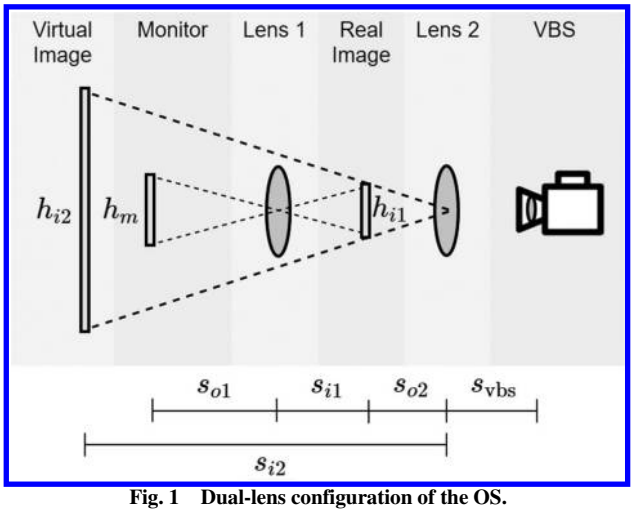

Fig. 1 Dual-lens configuration of the OS.

Note that an image distance s is negative if an object/image pair exists on the same side of a single lens. The magnification is negative ($M < 0$) if an image is inverted with respect to its corresponding object. To achieve a desired M, the values s_{i1} and s_{o1} need to be solved for. To solve for these variables, the thin lens equation is applied to lens 1 and lens 2 with focal lengths f_1 and f_2, as given next:

$$\frac{1}{f_1} = \frac{1}{s_{o1}} + \frac{1}{s_{i1}} \tag{6}$$

$$\frac{1}{f_2} = \frac{1}{s_{o2}} + \frac{1}{s_{i2}} \tag{7}$$

The virtual image produced by lens 2 is a synthetic composition of objects that would be encountered in the operational environment of the VBS. If the main feature to be synthesized is a NSO at some separation r, then the virtual image should be placed at $s_{i2} = -r$. If the operational environment is composed of SOs and/or NSOs at far ranges ($\geq$ 10 km), it is reasonable to assume that rays of light reaching the VBS from these sources are collimated (i.e., $s_{i2} = -\infty$). Given that s_{i2} is known for an operational environment, the placement of the intermediate real image can be solved for using

$$s_{o2} = \left(\frac{s_{i2}}{s_{i2} - f_2}\right) f_2 \tag{8}$$

which provides

$$\lim_{s_{i2} \to -\infty} s_{o2} = \lim_{s_{i2} \to -\infty} \left[\left(\frac{s_{i2}}{s_{i2} - f_2}\right) f_2\right] = f_2 \tag{9}$$

Equation (8) shows that $s_{o2} \leq f_2$ for $s_{i2} < 0$. This implies that, for operational scenarios of interest (i.e., $s_{i2} < 0$), the image produced by lens 2 is always a virtual image. Assuming that f_1 and f_2 are known, Eqs. (5) and (6) can be combined to solve for s_{o1} as

$$s_{o1} = \left(\frac{M - 1}{M}\right) f_1 \tag{10}$$

The variable s_{i1} can be solved for by combining Eqs. (5) and (10) as given by

$$s_{i1} = (1 - M) f_1 \tag{11}$$

A plot of the optical separations defined by Eqs. (10) and (11) versus magnification is shown in Fig. 2.

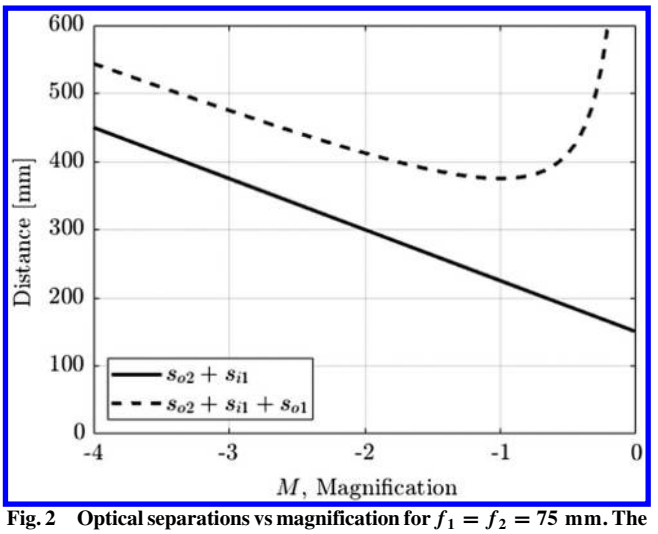

Fig. 2 Optical separations vs magnification for $f_1 = f_2 = 75$ mm. The solid line represents the distance between lenses 1 and 2, and the dotted line represents the distance between lens 2 and the monitor.

Because the OS uses variable magnification, parameters with a functional dependence on M need to be actuated (i.e., s_{o1} and s_{i1}). This requires two sets of relative motion: 1) between the monitor and lens 1, and 2) between lenses 1 and 2. To reduce the number of actuators, it is desired to keep the monitor or one of the two lenses stationary. The choice was made to keep lens 2 stationary, which reduces cabling complexity of the VBS test article.

A. Focal Length Analysis

The first factor considered in the selection of f_1 and f_2 is the overall size of the testbed, where the optical axis is anticipated to be the longest dimension of the testbed. An estimate of the overall length L of the testbed as a function of f_1 and f_2 is computed by calculating the farthest distance that the monitor would be from lens 2 for a desired range of $M \in [M_1, M_2]$, as given by

$$L(f_1, f_2) = \underset{M}{\text{maximize}}\ s_{o2} + s_{i1} + s_{o1} \quad \text{subject to } M_1 \le M \le M_2 \tag{12}$$

The solution to Eq. (12) for considered focal lengths is plotted in Fig. 3. A second factor considered in the selection of f_1 and f_2 is the actuation stroke requirements to achieve a desired magnification $M \in [M_1, M_2]$. The stroke requirement for actuating lens 1 (u_1) and the monitor (u_2) are solved for by considering the difference between the maximum and minimum distance an element needs to be placed for $M \in [M_1, M_2]$, as shown by

$$u_1(f_1, f_2) = \text{maximize}\ [\max_M(s_{o2} + s_{i1}) - \min_M(s_{o2} + s_{i1})] \quad \text{subject to } M_1 \le M \le M_2 \tag{13}$$

$$u_2(f_1, f_2) = \text{maximize}\ [\max_M(s_{o2} + s_{i1} + s_{o1}) - \min_M(s_{o2} + s_{i1} + s_{o1})] \quad \text{subject to } M_1 \le M \le M_2 \tag{14}$$

A third factor considered in the selection of f_1 and f_2 is the sensitivity of achievable magnification to actuation errors (Δs_{o1}) for a range of focal lengths. The sensitivity is quantified by analyzing variations in magnification ΔM due to Δs_{o1}, as shown by

$$\Delta M = \frac{\partial M}{\partial s_{o1}} \Delta s_{o1} \tag{15}$$

To compute $\partial M / \partial s_{o1}$, Eq. (10) is rearranged to a form that facilitates calculating $\partial M / \partial s_{o1}$, as shown by

$$M = \frac{f_1}{f_1 - s_{o1}} \tag{16}$$

$$\frac{\partial M}{\partial s_{o1}} = \frac{f_1}{(f_1 - s_{o1})^2} \tag{17}$$

Figure 3 shows the solutions of Eq. (15) when solved over a range of f_1 and M using Eqs. (10) and (17).

Figure 3 demonstrates that increasing f_2 impacts the growth of L less than increasing f_1. Although f_2 contributes to increasing L, it has no impact on u_1 and u_2. The advantage of longer f_1 is reduced sensitivity to actuation errors. The disadvantage is that longer f_1 increases L, u_1, and u_2.

B. Selected Hardware

The focal lengths selected for the OS are $f_1 = 75$ mm and $f_2 = 75$ mm. This achieves the desired magnification range of $M \in [-4, -0.25]$ with a reasonable testbed size and actuator stroke requirements. The lenses are 2-in.-diam achromatic doublets designed for use with visible wavelengths. The OS uses a pair of 400 mm linear stages driven by stepper motors to position lens 1 and the monitor with relative separations defined by Eqs. (10) and (11) for a given magnification level. Lens 1 and the monitor interface to their respective stepper motor carriages through a three-axis translational stage. These translational stages are used to position the elements along a common optical axis. The stepper motors are commanded with an Arduino microcontroller communicating with MATLAB/Simulink over a serial connection.

Post holders and a custom three-dimensional (3-D) printed bracket are used to align the optical axis of a VBS with the optical axis of lens 2 of the OS. These components also position the objective of the VBS at $s_{\text{vbs}} = 50$ mm. The geometry of the OS guarantees that the first lens is always defined as the entrance pupil. For the selected hardware and magnification range, the corresponding location of the exit pupil will always exist at a plane farther from the second lens than the aforementioned value of s_{vbs}. The smallest diameter of the exit pupil over the magnification range of interest was calculated to be 10.16 mm at $M = -4$. Hence, with this OS geometry and a VBS with an aperture of 10 mm or less, vignetting will never occur, and the VBS will always be overfilled. A VBS with a larger aperture will, however, limit the magnification range that can be supported by the OS.

An eMagin WUXGA ULT organic light-emitting diode (OLED) monitor was selected for its high resolution, contrast ratio, dynamic range, peak brightness, and small pixel pitch. This OLED monitor is

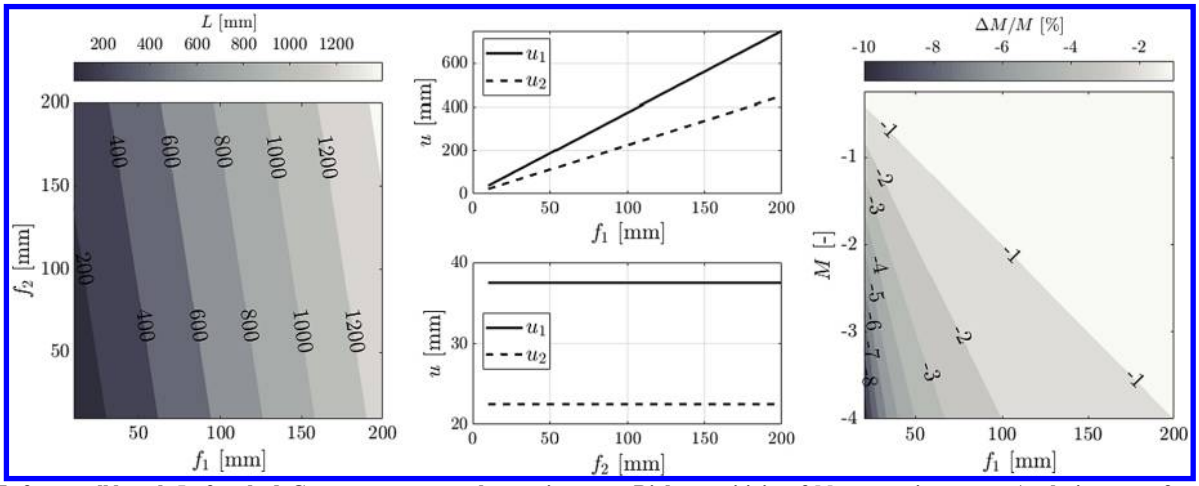

Fig. 3 Left: overall length L of testbed. Center: actuator stroke requirements. Right: sensitivity of M to actuation errors. Analysis was performed with $M \in [-4, -0.25]$.

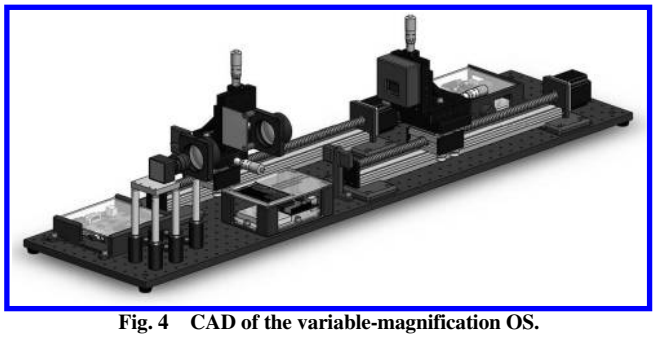

Fig. 4 CAD of the variable-magnification OS.

approximately 2×1 cm in size and is mounted on a printed circuit board containing driver electronics. This printed circuit board is housed in a 3-D-printed enclosure that interfaces to the three-axis translational stage. A computer-aided design of the variable-magnification OS using commercial-off-the-shelf components was created and is shown in Fig. 4. The actual testbed is shown in Fig. 5.

IV. Synthetic Scene Generation

The space environment is synthetically emulated by rendering 3-D vector graphics to the monitor that are created using Open Graphics Library (OpenGL) [35]. The visual magnitude, right ascension, declination, and proper motion of SOs are obtained from the Hipparcos star catalog [36]. These parameters are used in conjunction with the pose of the VBS to determine the intensity and location of an SO being rendered to the monitor. Stereolithography files of NSOs (satellites, asteroids, debris, planets, moons, etc.) are parsed into vertex arrays used in OpenGL application programming interface calls. The pose of these objects relative to the VBS is calculated using a high-fidelity numerical simulation of the underlying orbital and attitude dynamics [37]. A fragment shader then illuminates each of the model's triangular facets based on its pose relative to multiple light sources of variable radiometric intensity (i.e., sun, Earth albedo, moonlight, etc.) and configurable material properties. The OS software is written in C++, including MEX and s-function wrappers, which allow the core C++ functionality to be accessed through the MATLAB command terminal and in Simulink. Examples of synthetic images created by the OS software to recreate images with corresponding flight data from the PRISMA mission [38] are displayed in Fig. 6. Relative position and orientation of the VBS used for image generation were obtained from actual flight data for this dataset [38].

V. Calibration of Optical Stimulator

A. Geometric

The purpose of the geometric calibration is to stimulate the VBS from a simulated angular origin in the presence of optical distortions introduced by the COs. This is achieved by providing the rendering software with unit vectors, which are functions of VBS stimulus unit vectors and the intrinsic parameters of the COs. This relationship is modeled by

$$\boldsymbol{B} = \boldsymbol{A}\boldsymbol{X} \tag{18}$$

with

$$\boldsymbol{B} = \begin{bmatrix} x_1 & y_1 & z_1 \\ x_2 & y_2 & z_2 \\ & \vdots & \\ x_N & y_N & z_N \end{bmatrix}_{\text{os}} \tag{19}$$

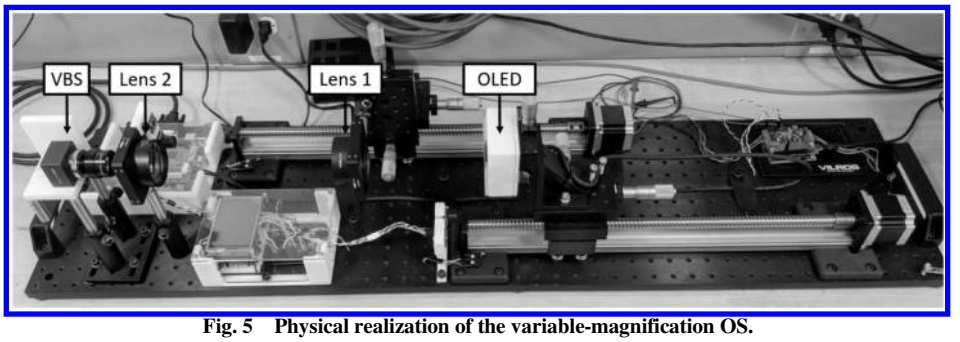

Fig. 5 Physical realization of the variable-magnification OS.

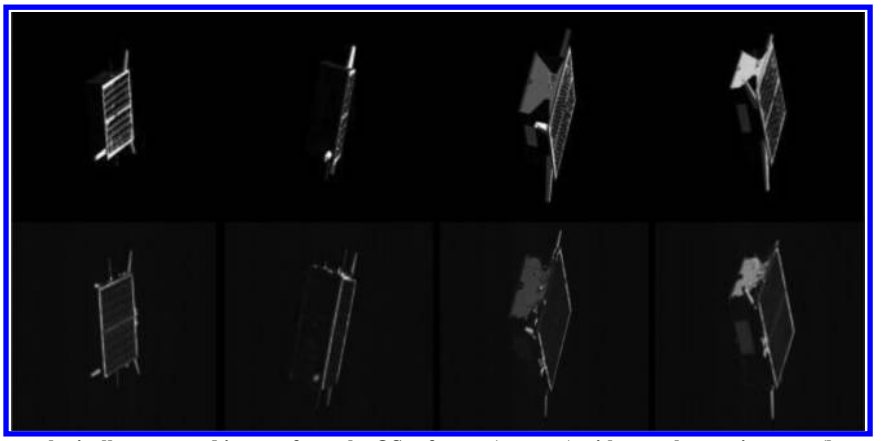

Fig. 6 Comparison of the synthetically generated images from the OS software (top row) with actual space imagery (bottom row) from the PRISMA mission [38].

$$\boldsymbol{A} = \begin{bmatrix} \left(\frac{x_1}{z_1}\right)^0\left(\frac{y_1}{z_1}\right)^0 & \left(\frac{x_1}{z_1}\right)^0\left(\frac{y_1}{z_1}\right)^1 & \cdots & \left(\frac{x_1}{z_1}\right)^m\left(\frac{y_1}{z_1}\right)^{m-1} & \left(\frac{x_1}{z_1}\right)^m\left(\frac{y_1}{z_1}\right)^m \\ \left(\frac{x_2}{z_2}\right)^0\left(\frac{y_2}{z_2}\right)^0 & \left(\frac{x_2}{z_2}\right)^0\left(\frac{y_2}{z_2}\right)^1 & \cdots & \left(\frac{x_2}{z_2}\right)^m\left(\frac{y_2}{z_2}\right)^{m-1} & \left(\frac{x_2}{z_2}\right)^m\left(\frac{y_2}{z_2}\right)^m \\ \vdots & \vdots & \ddots & \vdots & \vdots \\ \left(\frac{x_N}{z_N}\right)^0\left(\frac{y_N}{z_N}\right)^0 & \left(\frac{x_N}{z_N}\right)^0\left(\frac{y_N}{z_N}\right)^1 & \cdots & \left(\frac{x_N}{z_N}\right)^m\left(\frac{y_N}{z_N}\right)^{m-1} & \left(\frac{x_N}{z_N}\right)^m\left(\frac{y_N}{z_N}\right)^m \end{bmatrix}_{\text{vbs}} \tag{20}$$

$$\boldsymbol{X} = \begin{bmatrix} c_{0,0} & d_{0,0} & e_{0,0} \\ c_{0,1} & d_{0,1} & e_{0,1} \\ & \vdots & \\ c_{m,m-1} & d_{m,m-1} & e_{m,m-1} \\ c_{m,m} & d_{m,m} & e_{m,m} \end{bmatrix} \tag{21}$$

where c, d, and e are unknown coefficients modeling the intrinsic parameters of the COs using a polynomial of order m; $[\,x_i \quad y_i \quad z_i\,]_{\text{vbs}}$ is the ith unit vector for the measured VBS stimulus direction; and $[\,x_i \quad y_i \quad z_i\,]_{\text{os}}$ is the actuation vector passed to the OS rendering software. The matrix of unknown intrinsic parameters $\boldsymbol{X}$ can be estimated by solving Eq. (18) using a QR-based least-squares approach. This can be accomplished by rendering a calibration grid of dots to the OS monitor (i.e., $\boldsymbol{B}$ is known) and populating the matrix $\boldsymbol{A}$ using a VBS-acquired image of the calibration pattern.

Because the intrinsic parameters are function of the intercomponent separation, these coefficients need to be estimated at several discrete magnification levels. Linear interpolation of the intrinsic parameters can be used when operating at some intermediate magnification level M, where a calibration was not explicitly performed. Given that $\boldsymbol{X}_1$ was estimated for a magnification M_1, and $\boldsymbol{X}_2$ was estimated for a magnification M_2, the matrix $\boldsymbol{B}$ to be commanded to the OS can be computed from

$$\boldsymbol{B} = A\tilde{\boldsymbol{X}} \tag{22}$$

where

$$\tilde{\boldsymbol{X}} = \left(1 - \frac{M - M_1}{M_2 - M_1}\right)\boldsymbol{X}_1 + \left(\frac{M - M_1}{M_2 - M_1}\right)\boldsymbol{X}_2 \tag{23}$$

The quality of the calibration was assessed by rendering a grid of dots to the OS monitor to stimulate a VBS calibration article with a desired set of unit vectors, using Eq. (22). Angular residuals $d\theta$ were computed as the inner angle between desired and measured unit vectors for each dot in the rendered grid and are plotted in Fig. 7.

Figure 7 shows a decrease in the average magnitude of $d\theta$ as M decreases. This is expected because a magnified OS monitor pixel subtends a larger solid angle in the VBS's FOV. As M decreases, the OS monitor pixel subtends a smaller solid angle and eventually drops below the angular precision that can be measured by the VBS calibration article. Because of this phenomenon, the OS can only be geometrically calibrated to the angular precision of the VBS calibration article. These results show that the OS can consistently place point sources of light within $10''$ or better in the presence of varying distortion for a wide range of M.

B. Radiometric

The objective of the radiometric calibration is to characterize the functional relationship between the scene rendered to the monitor and the irradiance arriving at the aperture of the VBS as M varies. A ThorLabs S130C high-resolution optical power meter was placed at the plane where the VBS aperture normally would be and was used to measure the radiometric flux. Irradiance measurements were gathered at different wavelengths by varying the OS magnification level and monitor digital count. These measurements were used to identify the irradiance through the OS as a function of OS monitor state and magnification level. Irradiance measurements per OS monitor pixel obtained at varying monitor digital count are plotted in Fig. 8. Measurements were obtained with the central 1% of the OS monitor pixels illuminated and the exit pupil of the OS overfilling the optical power meter. These curves normalize the measurement obtained by the number of OS illuminated monitor pixels to estimate the irradiance contribution from a single OS monitor pixel.

As shown in Fig. 8, the radiometric dynamic range of an OS monitor pixel changes as a function of magnification. By transitioning from $M = -0.25$ to $M = -4$, the peak irradiance increases by a factor of 10 within a color channel. When using a single monitor pixel at low digital count, the OS has the ability to stimulate VBSs with point sources of light near 10^{-12} W $\cdot$ m^{-2} and can simulate sources up to 10^{-4} W $\cdot$ m^{-2} when magnified and using multiple pixels at high digital count. This represents a radiometric dynamic range spanning eight orders of magnitude.

VI. Results

Two HIL experiments were conducted using the variable-magnification OS to stimulate a far- and close-range VBS. The far-range VBS has a narrow FOV and is used in an AON scenario, and the close-range VBS with a wide FOV is used in a pose estimation scenario. The parameters of these two VBSs are outlined in Table 3.

A. Angles-Only Navigation

The first test scenario considered in this work looks at the problem of relative navigation of an observing spacecraft with respect to a NSO in a near-circular, low Earth orbit (LEO). In this configuration, the observer spacecraft is attempting to estimate the relative orbital motion of the target space object using only bearing angles obtained by a far-range VBS (9 deg diagonal FOV). AON represents an especially difficult estimation scenario due to the inherent dynamical observability constraints imposed by using bearing angle measurements

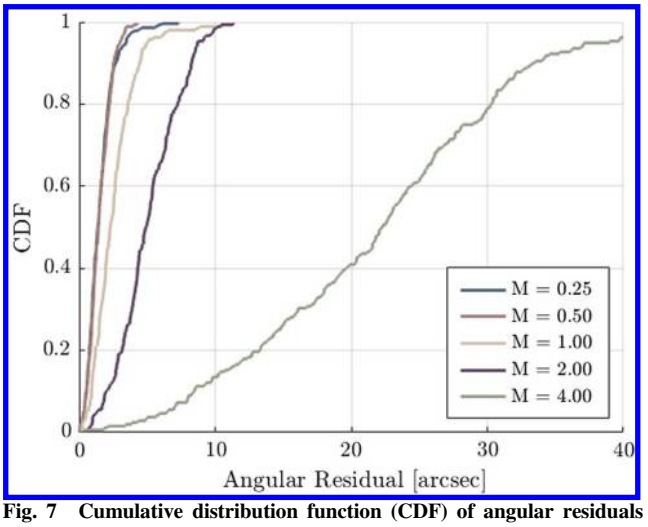

Fig. 7 Cumulative distribution function (CDF) of angular residuals between desired and measured feature locations at several magnification levels.

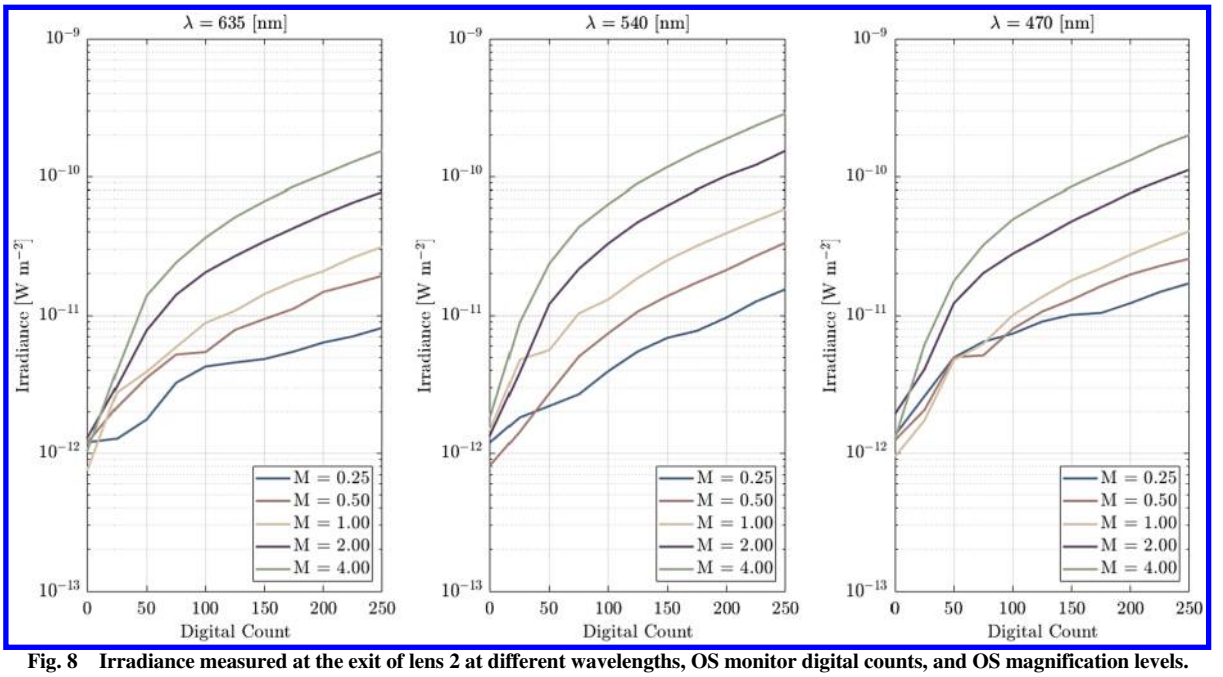

Fig. 8 Irradiance measured at the exit of lens 2 at different wavelengths, OS monitor digital counts, and OS magnification levels.

(two-dimensional) to reconstruct the full relative orbital motion state (six-dimensional). For this test scenario, the NSO relative orbital motion is chosen to be similar to the scenarios considered by Sullivan et al. [18]. In that work, the authors use a set of relative orbital elements (ROEs) consisting of the relative semimajor axis δa, relative mean longitude $\delta\lambda$, and relative eccentricity and inclination vectors $\delta\boldsymbol{e}$ and $\delta\boldsymbol{i}$ to parameterize the relative motion of the NSO with respect to the observing spacecraft [39]. The initial conditions for the observing spacecraft and the relative motion of the NSO are provided in Table 4.

For simplicity but without loss of generality, the VBS on the observing spacecraft is assumed to be pointing with a fixed boresight alignment in the antiflight direction. Beginning from the specified initial conditions, the absolute position and velocity of the observing spacecraft and target NSO are numerically propagated for several orbits using a high-fidelity simulator that includes rigorous force models of high-order gravity, atmospheric drag, solar radiation pressure, third-body sun and moon effects, and tidal effects [37]. The numerically propagated trajectories provide the ground truth against which to compare the performance of the AON filter. To estimate the relative orbit of the NSO, the filter requires knowledge of both the observer absolute orbital state and VBS-frame absolute attitude, as well as sequential sets of bearing angles that subtend the line-of-sight vector pointing from the observer to the NSO. The observer absolute orbit knowledge is provided by corrupting the ground truth observer orbit with measurement noise that is representative of coarse position/velocity/time solutions obtained using a global positioning system receiver. Instead, the HIL VBS stimulated by the OS provides the measured attitude and bearing angles. The relationship between the bearing angles and the relative position is illustrated in Fig. 9.

A simplified architectural layout of the AON algorithm is depicted in Fig. 10. Regions of interest obtained from the far-range VBS are fed into an image processing algorithm to detect and link clusters of bright pixels. Using the Hipparcos star catalog, a star identification process labels some of these clusters as SOs and produces an inertial attitude estimate q. The remaining bright clusters are taken to be NSO candidates. Prior information on the orbital elements $\boldsymbol{oe}$ of the observer and target NSO are assumed to be available. This absolute orbit knowledge aides in the selection of the NSO candidate to be navigated relative to. A line-of-sight vector to the NSO is used to compute bearing measurements α, ε, which are fed into an unscented Kalman filter (UKF) formulated by Sullivan and D'Amico [19,20]. The UKF returns an estimate of the relative orbital elements $\delta\boldsymbol{oe}$ to the NSO and covariance matrix $\boldsymbol{P}$.

With the navigation architecture presented in Fig. 10, the filter is able to converge to a very good estimate of the relative orbit of the NSO, demonstrating steady-state estimation error within 2.5% of the true mean interspacecraft range (as given by $a\delta\lambda$) and to within 10 m for all other state elements, as shown in Fig. 11. A comparison of the angles-only filter prefit and postfit measurement residual steady-state statistics in Table 5 indicate worst-case postfit residuals for azimuth and elevation at approximately 8 and 22% of the iFOV associated with a test article pixel, respectively. This is a strong indication that the filter is processing measurements effectively and reducing modeling residuals to the noise floor of the onboard sensor. It is instructive to mention that the larger standard deviation in the elevation angle postfit residuals is expected because the range ambiguity translates to an elevation error in filter modeling due to the orbit curvature. To the

Table 3 Specifications for the far- and close-range VBSs used in the HIL experiments

Parameter	Far range	Close range
Model	Matrix Vision BlueFox	Point Grey Grasshopper
Focal length, mm	35	17.6
Pixel pitch, μm/pixel	9.6	2.2
Dimensions, pixels	2048×1536	1920×1200
FOV, deg	7.37×5.53	35.45×22.59

Table 4 Initial observer orbital conditions and mean ROE test case for dynamic simulation

Observer orbit	$a = 7200$ km	$e = 0.001$	$i = 30$ deg	$\Omega = 60$ deg	$\Omega = 120$ deg	$M_0 = 0$ deg
Initial ROE, m	$a\delta a$	$a\delta\lambda$	$a\delta e_x$	$a\delta e_y$	$a\delta i_x$	$a\delta i_y$
ROE 2	−50	−10,000	200	0	−200	0

authors' knowledge, this is the first published HIL result of a completely maneuver-free, stable, and converging AON filter using a synthetic stimulus. This HIL implementation of an AON filter demonstrates the utility of the OS testbed for investigating functionality and performance in different operational environments.

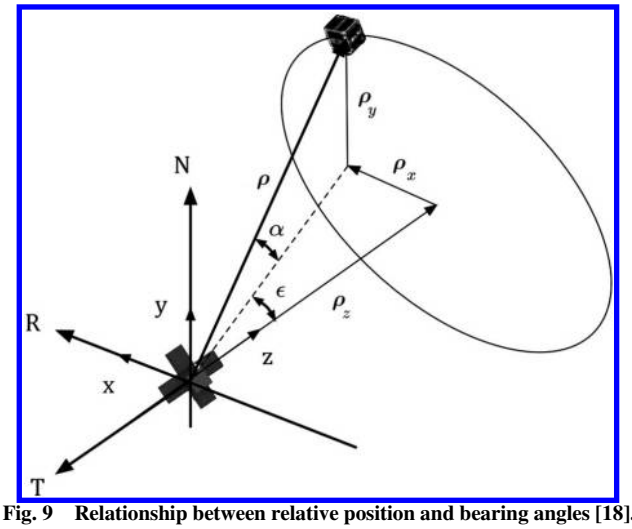

Fig. 9 Relationship between relative position and bearing angles [18].

Table 5 Statistics of the VBS and filter residuals for the 7 dynamic relative navigation simulation over the last three simulated orbits

Residual	$\bar{\Delta\alpha} \pm 1\sigma$, arcsec	$\bar{\Delta\epsilon} \pm 1\sigma$, arcsec
VBS	$+1.62 \pm 04.09$	-3.56 ± 03.92
Prefit	-2.58 ± 36.76	-5.18 ± 58.22
Postfit	-0.89 ± 01.77	$+1.03 \pm 07.00$

At intersatellite separations on the order of kilometers, azimuth and elevation measurements calculated from the image processing algorithm were experimentally observed to be accurate and precise ($1\sigma = 10.3''$). As the intersatellite separation decreases to hundreds of meters, features (i.e., antennas, solar panels, etc.) on the observed satellite and its structure start to become visible. Illumination and shadowing of the observed satellite dynamically change as a function of the NSO's pose relative to the observing VBS, sun, and Earth. When using a simple center-of-mass image processing centroiding algorithm, shadowing and varying illumination of the observed satellite result will degrade the accuracy of the measured bearing angles. This phenomenon can be observed in Fig. 12.

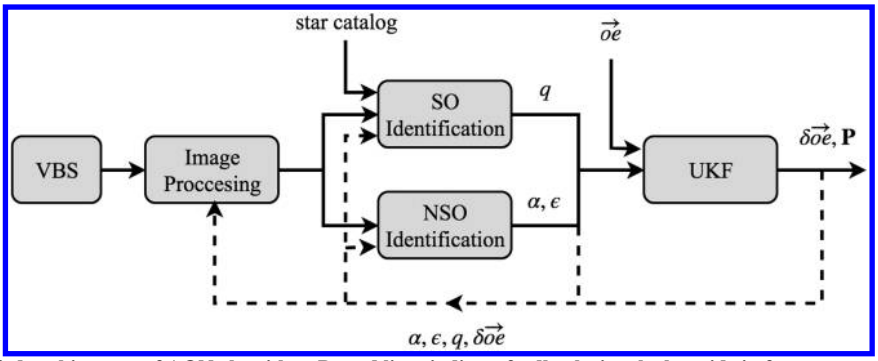

Fig. 10 Simplified architecture of AON algorithm. Dotted lines indicate feedback signals that aide in future execution of processes.

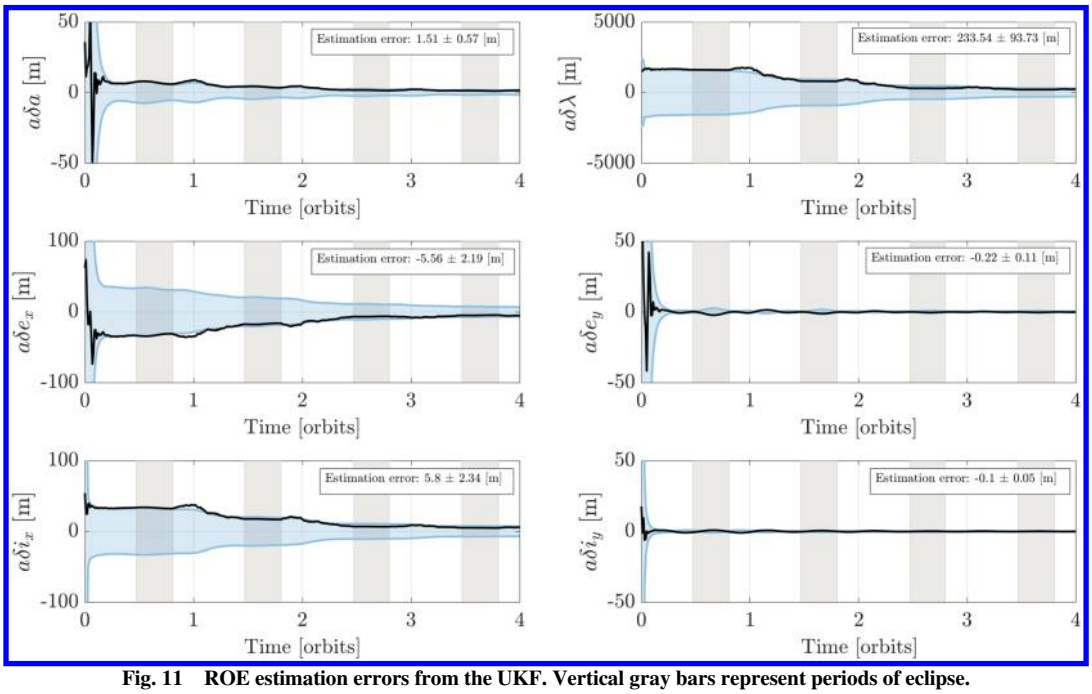

Fig. 11 ROE estimation errors from the UKF. Vertical gray bars represent periods of eclipse.

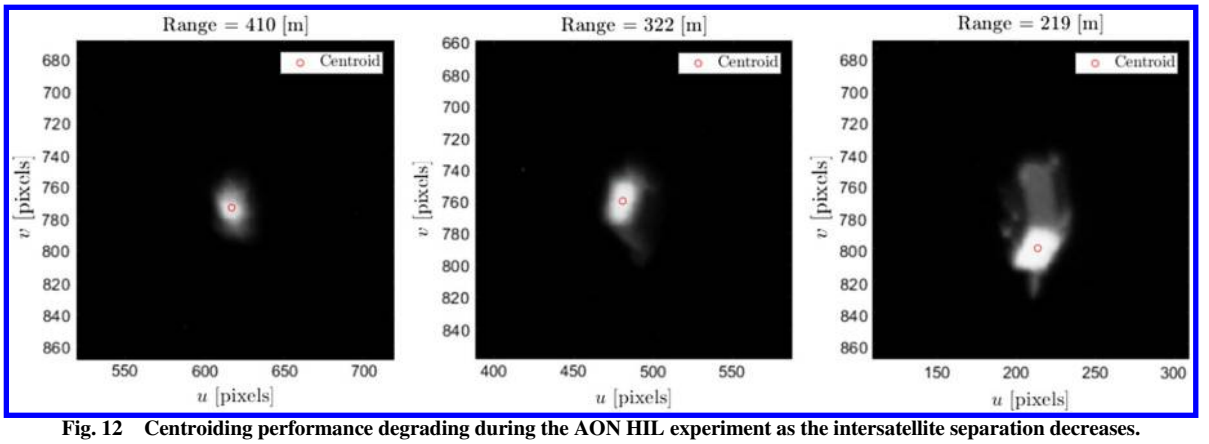

Fig. 12 Centroiding performance degrading during the AON HIL experiment as the intersatellite separation decreases.

B. Pose Determination

The second test scenario considers an observing satellite with a close-range VBS (outlined in Table 3) formation flying in close proximity (10–20 m intersatellite separation) to the Tango satellite from the PRISMA mission. The observing satellite is attempting to estimate the relative position and orientation, or pose, of the Tango satellite using a single monocular image. The synthesized scenes rendered to the OS monitor stimulate a close-range VBS on the observing satellite, which is estimating the relative pose of Tango using a deep convolutional neural network (CNN) formulated by Sharma et al. [40,41]. In that work, the authors divide the continuous six-dimensional pose space into discrete bins and solve a classification problem to determine the relative pose of Tango, as shown in Fig. 13. The pose label predicted by the CNN corresponds to a region in a four-dimensional space. Of these four dimensions, three correspond to the attitude of the VBS reference frame with respect to the Tango body reference frame, and one corresponds to the distance from the origin of the VBS reference frame to the origin of the Tango body reference frame. The output of the last fully connected layer of the CNN is passed through the softmax function, yielding values that can be interpreted as the probability of the image being associated to each pose label.

Training of the CNN was accomplished by generating a large dataset consisting of several thousand labeled images acquired with the close-range VBS being stimulated by the OS. The automated pipeline for generation and labeling of space imagery is based on uniformly discretizing the four-dimensional viewspace around a target object. Uniformly distributing a set of n VBS locations around the target is akin to solving for a minimum-energy configuration for charged particles on a sphere of radius r. The determination of this stable configuration of particles constrained on a sphere and being acted on by an inverse square repelling force is known as the Thomson problem [42]. Using this approach to solve for the uniform distribution of points on a sphere fixes two of the four degrees of freedom in the view space. The third degree of freedom is the rotation of the VBS about the boresight direction, which can be uniformly discretized in $m - 1$ intervals from 0 to 360 deg. Finally, the degree of freedom corresponding to the distance of the VBS relative to the target can be discretized by generating spheres of varying radii. Figure 14 illustrates the discretization of the continuous attitude space into various classes.

The trained CNN is then used to estimate the relative pose on a validation set not used during training. Angular residuals between the CNN predicted attitude and the ground truth attitude used in the OS rendering pipeline are parameterized with a set of 3-2-1 Euler angles. For small residuals, these Euler angles correspond to rotations about the axes of the VBS frame (the first and second axes are the horizontal and vertical directions of the image plane, the third axis is boresight direction). Range residuals are computed by simply differencing the ground truth and CNN predicted range. A wireframe model of the Tango satellite corresponding to the predicted poses is plotted on top of the HIL acquired images in Fig. 15. The plots include annotations with the aforementioned residuals, along with a pose class confidence metric coming from the CNN computed softmax probabilities.

The trained CNN was then used to estimate the pose of the Tango satellite in a sequence of images recreating an hour-long segment of flight data (starting at 6 Oct. 2011 22:49:16 GPS time) obtained from the PRISMA mission [38]. Specifically, on-ground precise relative

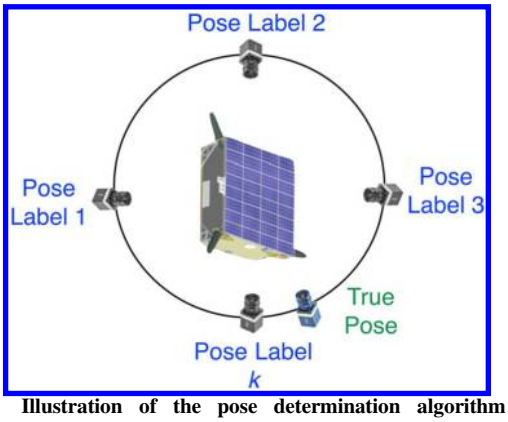

Fig. 13 Illustration of the pose determination algorithm as a classification problem.

Fig. 14 Illustration of the attitude discretization approach. The black dots represent pose classes, whereas the colored markers represent the poses corresponding to the nearest pose class.

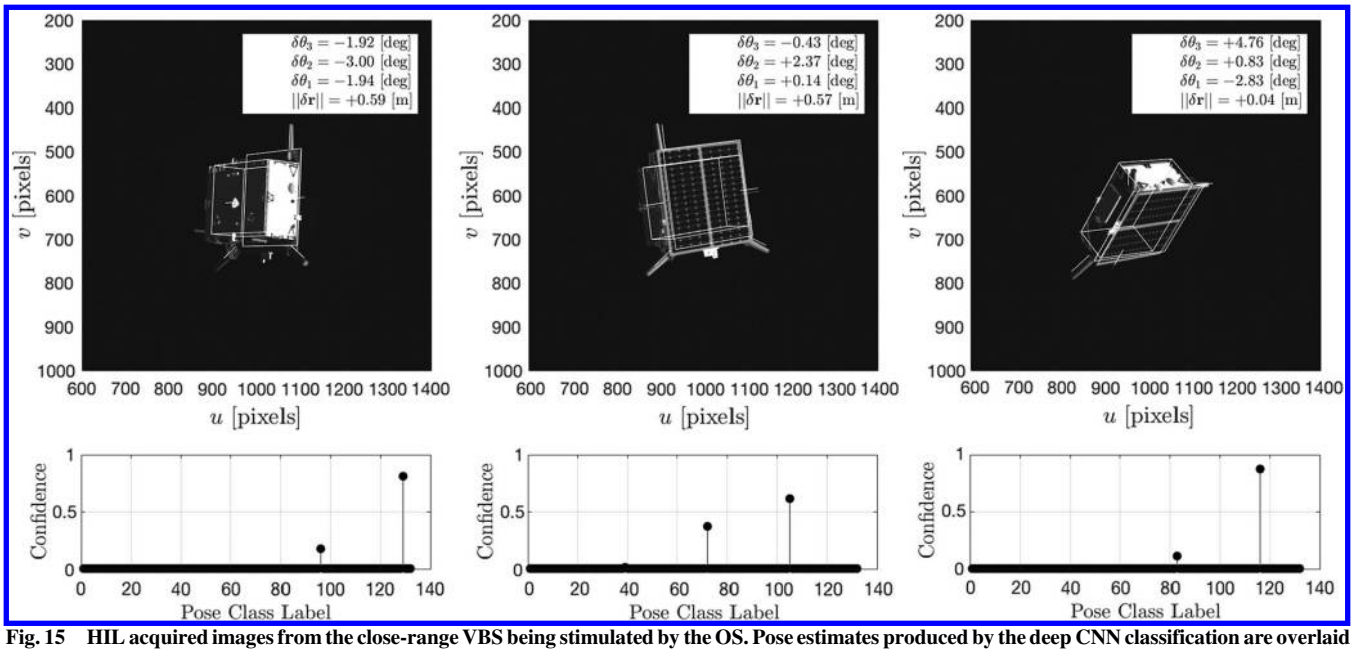

Fig. 15 HIL acquired images from the close-range VBS being stimulated by the OS. Pose estimates produced by the deep CNN classification are overlaid using a wireframe model of Tango.

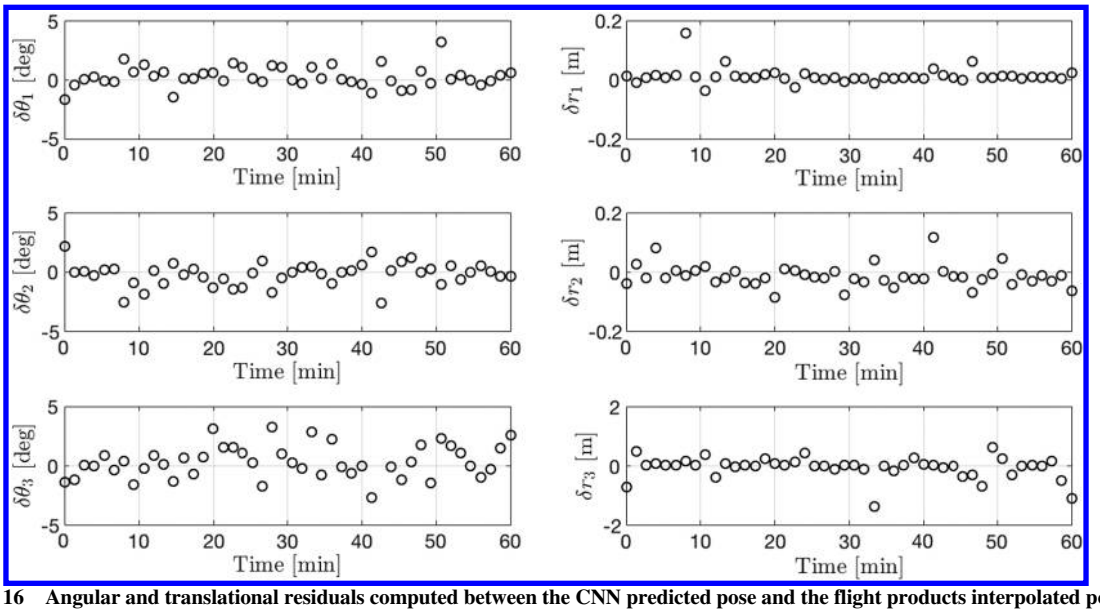

Fig. 16 Angular and translational residuals computed between the CNN predicted pose and the flight products interpolated pose.

orbit determination based on GPS (accurate to about 2 cm 3-D rms) [43] is used as the true relative position. The onboard attitude estimate provided by star trackers aboard the Mango satellite and a combination of sun sensors and magnetometers aboard the Tango satellite (accurate to about 3 deg 3-D rms) are used to calculate the relative attitude between the VBS frame and Tango body axes. The relative pose, absolute orbit, and timing information obtained from the PRISMA flight products are used as inputs in the synthetic image generation pipeline of the OS. Pose computed by the CNN on this sequence of images was compared against the interpolated flight data to produce a sequence of translational and angular residuals. The aforementioned interpolation scheme used SLERP [44] for interpolating attitude and a 12th-order Lagrangian interpolation [45] for interpolating position between data in the flight products. These residuals are plotted in Fig. 16.

As shown in Fig. 16, the pose determined by the CNN is able to reach accuracies consistent with the discretization of the pose space (degree and centimeter level). This is achieved with only 5000 training images. This same CNN was then stress tested by attempting to determine the pose of Tango with the Earth in the background. As the position of the sun relative to the Earth evolves during this test, light from Earth albedo causes many pixels to register high digital counts, as shown in Fig. 17. Note that the accuracy and confidence of the pose estimate degrades as the Earth is observed brighter in the background in Fig. 17.

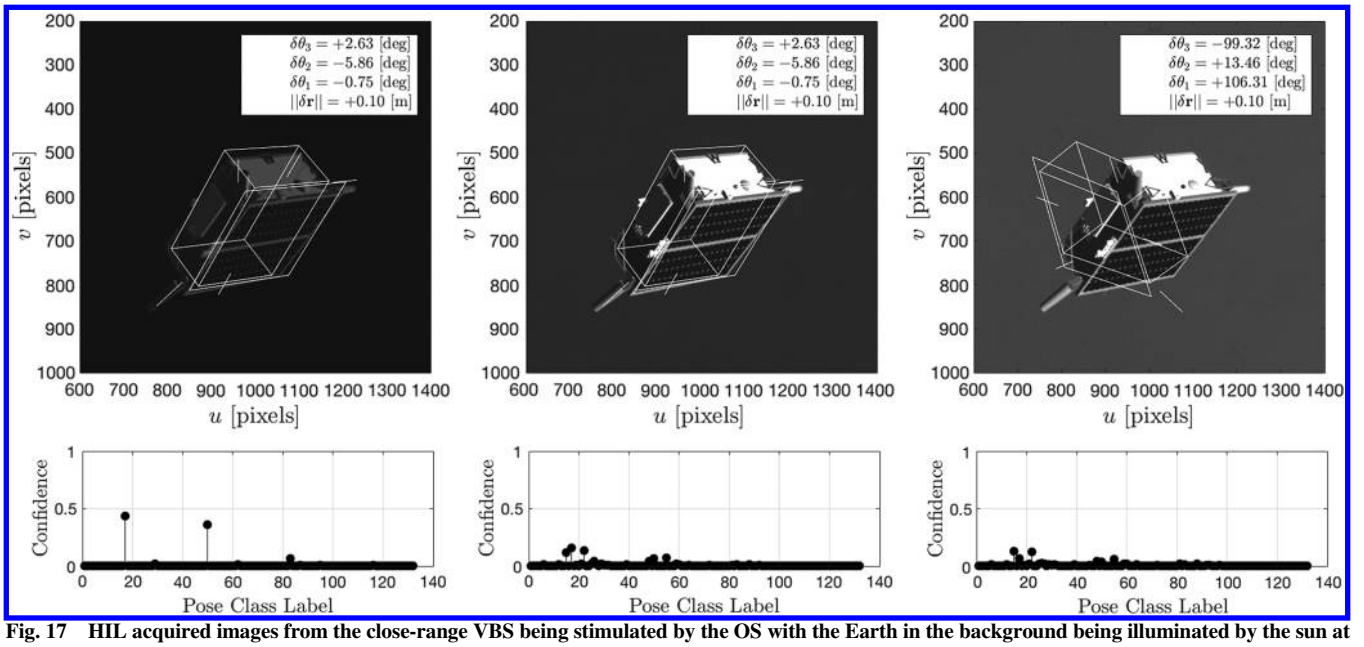

Fig. 17 HIL acquired images from the close-range VBS being stimulated by the OS with the Earth in the background being illuminated by the sun at different angles.

VII. Conclusions

This paper addresses the design, calibration, and utilization of a hardware-in-the-loop (HIL) testbed to stimulate optical hardware for spaceborne vision-based navigation. The assembled testbed and selected components were converged upon through a design process to meet an explicit set of functional and performance requirements to simulate simulate stellar objects (SOs) and nonstellar objects (NSOs) from a geometric and radiometric standpoint and support testing of vision-based sensors (VBSs) with narrow and wide FOV. The variable-magnification optical stimulator (OS) consists of an organic light-emitting diode (OLED) monitor stimulating a VBS through a pair of lenses. The relative positioning of these components is achieved using two motorized stages that translate the OLED monitor and one of the lenses along the optical axis of the testbed. This approach is shown to support VBSs of both narrow and wide FOV, increase the radiometric dynamic range of the testbed, and emulate close-range scenarios when light from an object is not collimated. Geometric calibration of the testbed consisted of isolating the distortions introduced by the lenses of the OS and warping the scene rendered to the monitor to produce a stimulus reaching the aperture of the VBS test article from the intended angular location. A radiometric calibration quantified the irradiance of an OS monitor pixel as a function of digital count and testbed magnification. These calibration steps were necessary to be able to accurately place simulated sources of light to within arcseconds of angular accuracy over a large radiometric dynamic range.

Two HIL experiments were conducted to illustrate the utility of the OS at verifying the functionality and performance of a VBS used for spaceborne navigation. The first HIL test simulated a formation-flying scenario to verify the functionality and performance of an angles-only navigation (AON) algorithm. The relative navigation algorithm uses measurements from a far-range VBS (9 deg diagonal FOV) collected by an observer spacecraft performing far-range rendezvous with a noncooperative client in LEO. These HIL observations were used to produce a sequence of inertial attitude measurements as well as bearing measurements to the NSO, whose relative position is unknown to the observing vehicle. This vision-based rendezvous scenario has a documented unobservability in discerning the relative separation that can be circumvented through the use of an angles-only filter. The high-dynamic range OS was able to accurately reproduce both SOs and the NSO from a geometric and radiometric standpoint simultaneously to stimulate the VBS test article in a realistic manner. The angles-only relative navigation algorithm was verified by assessing functional performance of the estimation solution and filter measurement modeling accuracy.

The second HIL test scenario considers an observing satellite with a monocular close-range VBS (42 deg diagonal FOV) formation flying in close proximity (10−20 m intersatellite separation) to the Tango satellite from the PRISMA mission. The relative pose, absolute orbit, and timing information obtained from PRISMA flight products are used as inputs in the synthetic image generation pipeline of the OS. Variable magnification of the OS is used to support testing of the wider FOV close-range VBS by translating components in accordance with the material presented in Sec. III. The stimulus provided by the OS allows for realistic images to be acquired by the close-range VBS test article. These HIL-acquired monocular images are fed into a deep convolutional neural network (CNN) that is attempting to estimate the relative pose of Tango, which is unknown to the observing vehicle. The CNN estimates the pose of Tango by producing a pose label classification, which corresponds to a discrete bin in the space of continuous poses observed during training of the CNN. In this experiment, the OS is used to stimulate the close-range VBS with a realistic stimulus and produce several thousand HIL images necessary for training of the CNN. At test time, the close-range VBS is stimulated by the OS with new scenes not encountered during training. These scenes are produced by interpolating with relative pose, absolute orbit, and timing information obtained from the PRISMA flight products. This close-range HIL training and testing enabled by the OS was used to verify the functional performance of the CNN pose estimator and quantify its performance accuracy. Future work includes using the OS to abridge the transition from AON to pose determination using HIL.

Acknowledgments

The work was supported in part by the U.S. Air Force Research Laboratory's Control, Navigation, and Guidance for Autonomous Spacecraft contract FA9453-16-C-0029 and by King Abdulaziz City for Science and Technology. The authors would like to express their appreciation to Josh Sullivan, Sumant Sharma, Adam Koenig, Andrew Norton, and Bruce Macintosh who all contributed to the advancement of this testbed. The authors would also like to thank OHB Sweden, DLR, and DTU for the PRISMA images used in this work.

References

[1] Roscoe, C. W., Westphal, J. J., Lutz, S., and Bennett, T., "Guidance, Navigation, and Control Algorithms for Cubesat Formation Flying," *38th AAS Guidance and Control Conference*, Advances in the Astronautical Sciences, American Astronautical Soc., Springfield, VA, Vol. 154, 2015, pp. 685–699.

[2] Christian, J., Patangan, M., Hinkel, H., Chevray, K., and Brazzel, J., "Comparison of Orion Vision Navigation Sensor Performance from STS-134 and the Space Operations Simulation Center," *AIAA Guidance, Navigation, and Control Conference*, AIAA Paper 2012-5035, Aug. 2012.
doi:10.2514/6.2012-5035

[3] D'Amico, S., Ardaens, J.-S., Gaias, G., Benninghoff, H., Schlepp, B., and Jørgensen, J. L., "Noncooperative Rendezvous Using Angles-Only Optical Navigation: System Design and Flight Results," *Journal of Guidance, Control, and Dynamics*, Vol. 36, No. 6, Sept. 2013, pp. 1576–1595.
doi:10.2514/1.59236

[4] D'Amico, S., Ardaens, J.-S., Gaias, G., Schlepp, B., Benninghoff, H., Tzschichholz, T., Karlsson, T., and Jørgensen, J. L., "Flight Demonstration of Non-Cooperative Rendezvous Using Optical Navigation," *23rd International Symposium on Space Flight Dynamics*, ISSFD Paper FF1-2, Pasadena, CA, 2012, http://issfd.org/ISSFD_2012/ISSFD23_FF1_2.pdf.

[5] Kolmas, J., Banazadeh, P., Koenig, A. W., D'Amico, S., and Macintosh, B., "System Design of a Miniaturized Distributed Occulter/Telescope for Direct Imaging of Star Vicinity," *Yellowstone Conference Center*, IEEE, New York, INSPEC Accession Number: 16121814, 2016.
doi:10.1109/AERO.2016.7500783.

[6] Seager, S., Cash, W., Domagal-Goldman, S., Kasdin, N. J., Kuchner, M., Roberge, A., Shaklan, S., Sparks, W., Thomson, M., Turnbull, M., et al., "Exo-S: Starshade Probe-Class Exoplanet Direct Imaging Mission Concept Final Report," NASA Rept. CL 15-1155, March 2015.

[7] Sanchez, H., McIntosh, D., Cannon, H., Pires, C., Sullivan, J., O'Connor, B., and D'Amico, S., "Starling1: Swarm Technology Demonstration," *32nd Annual Small Satellite Conference*, AIAA/USU, SSC18-VII-08, Logan, UT, 2018, https://digitalcommons.usu.edu/cgi/viewcontent.cgi?article=4111&context=smallsat.

[8] Strange, N., Landau, D., McElrath, T., Lantoine, G., and Lam, T., "Overview of Mission Design for NASA Asteroid Redirect Robotic Mission Concept," *33rd International Electric Propulsion Conference (IEPC2013)*, Jet Propulsion Lab., National Aeronautics and Space Administration, Pasadena, CA, Oct. 2013, http://hdl.handle.net/2014/44361.

[9] Brophy, J. R., and Muirhead, B., "Near-Earth Asteroid Retrieval Mission (Arm) Study," *33rd International Electric Propulsion Conference*, Jet Propulsion Lab., National Aeronautics and Space Administration, Pasadena, CA, Oct. 2013, http://hdl.handle.net/2014/44323.

[10] Boshuizen, C., Mason, J., Klupar, P., and Spanhake, S., "Results from the Planet Labs Flock Constellation," *Conference on Small Satellites*, AIAA Paper SSC14-I-1, 2014.

[11] Linskens, H., and Mooij, E., "Tether Dynamics Analysis and Guidance and Control Design for Active Space-Debris Removal," *Journal of Guidance, Control, and Dynamics*, Vol. 39, No. 6, 2016, pp. 1232–1243.
doi:10.2514/1.G001651

[12] Deloo, J., and Mooij, E., "Active Debris Removal: Aspects of Trajectories, Communication and Illumination During Final Approach," *Acta Astronautica*, Vol. 117, Aug. 2015, pp. 277–295.
doi:10.1016/j.actaastro.2015.08.001

[13] Gregory, D., Mergen, J.F., and Aaron, R., "Space Debris Elimination (SpaDE) Phase I Final Report," NASA Rept. NIAC-11-11NIAC-0241, 2012, https://www.nasa.gov/sites/default/files/atoms/files/niac_2011_phasei_gregory_spade_tagged.pdf [retrieved 22 June 2018].

[14] Reed, B. B., Smith, R. C., Naasz, B. J., Pellegrino, J. F., and Bacon, C. E., "The Restore-L Servicing Mission," *AIAA SPACE 2016*, AIAA Paper 2016-5478, 2016.
doi:10.2514/6.2016-5478

[15] Wenberg, D. L., Keegan, B. P., Lange, M. E., Hanlon, E. A., and Kang, J. S., "RSat Flight Qualification and Test Results for Manipulable Robotic Appendages Installed on 3U CubeSat Platform," *Conference on Small Satellites*, AIAA Paper SSC16-WK-42, 2016.

[16] Woffinden, D. C., and Geller, D. K., "Relative Angles-Only Navigation and Pose Estimation for Autonomous Orbital Rendezvous," *Journal of Guidance, Control, and Dynamics*, Vol. 30, No. 5, 2007, pp. 1455–1469.
doi:10.2514/1.28216

[17] Woffinden, D. C., and Geller, D. K., "Observability Criteria for Angles-Only Navigation," *IEEE Transactions on Aerospace and Electronic Systems*, Vol. 45, No. 3, 2009, pp. 1194–1208.

[18] Sullivan, J., Koenig, A., and D'Amico, S., "Improved Maneuver-Free Approach to Angles-Only Navigation for Space Rendezvous," *26th AAS/AIAA Space Flight Mechanics Meeting*, AAS Paper 16-530, Springfield, VA, 2016, https://people.stanford.edu/damicos/sites/default/files/aassfm2016_sullivankoenigdamico.pdf [retrieved 22 June 2018].

[19] Sullivan, J., and D'Amico, S., "Adaptive Filtering for Maneuver-Free Angles-only Navigation in Eccentric Orbits," *27th AAS/AIAA Space Flight Mechanics Conference*, AAS Paper 17-402, Springfield, VA, 2017, https://people.stanford.edu/damicos/sites/default/files/sfm2017_sullivandamico.pdf [retrieved 22 June 2018].

[20] Sullivan, J., and D'Amico, S., "Nonlinear Kalman Filtering for Improved Angles-Only Navigation Using Relative Orbital Elements," *Journal of Guidance, Control, and Dynamics*, Vol. 40, No. 9, 2017, pp. 2183–2200.

[21] Gaias, G., D'Amico, S., and Ardaens, J.-S., "Angles-Only Navigation to a Noncooperative Satellite Using Relative Orbital Elements," *Journal of Guidance, Control, and Dynamics*, Vol. 37, No. 2, 2014, pp. 439–451.
doi:10.2514/1.61494

[22] Ardaens, J.-S., and Gaias, G., "Spaceborne Autonomous Vision-Based Navigation System for AVANTI," *Proceedings of the 65th International Astronautical Congress*, Toronto, 2014, Paper 24852, http://iafastro.directory/iac/paper/id/24852/abstract-pdf/IAC-14,B4,7B,3,x24852.brief.pdf?2014-04-10.17:08:38.

[23] Leinz, M., Chen, C.-T., Beaven, M. W., Weismuller, T. P., Caballero, D. L., Gaumer, W. B., Sabasteanski, P. W., Scott, P. A., and Lundgren, M. A., "Orbital Express Autonomous Rendezvous and Capture Sensor System (ARCSS) Flight Test Results," *Proceedings of SPIE*, Vol. 6958, 2008, Paper 69580A.
doi:10.1117/12.779595

[24] Petit, A., Marchand, E., and Kanani, K., "Vision-Based Space Autonomous Rendezvous: A Case Study," *2011 IEEE/RSJ International Conference on Intelligent Robots and Systems*, IEEE Paper 978-1-61284-456-5/11, New York, 2011, pp. 619–624.
doi:10.1109/IROS.2011.6048176

[25] D'Amico, S., Benn, M., and Jørgensen, J. L., "Pose Estimation of an Uncooperative Spacecraft from Actual Space Imagery," *International Journal of Space Science and Engineering*, Vol. 2, No. 2, 2014, pp. 171.
doi:10.1504/IJSPACESE.2014.060600.

[26] Sharma, S., and D'Amico, S., "Reduced-Dynamics Pose Estimation for Non-Cooperative Spacecraft Rendezvous Using Monocular Vision," *38th AAS Guidance and Control Conference*, AAS Paper 17-073, Springfield, VA, 2017.

[27] Rufino, G., and Moccia, A., "Laboratory Test System for Performance Evaluation of Advanced Star Sensors," *Journal of Guidance, Control, and Dynamics*, Vol. 25, No. 2, 2002, pp. 200–208.
doi:10.2514/2.4888

[28] Boone, B. G., Bruzzi, J. R., Dellinger, W. F., Kluga, B. E., and Strobehn, K. M., "Optical Simulator and Testbed for Spacecraft Star Tracker Development," *Optical Modeling and Performance Predictions II*, edited by M. A. Kahan, SPIE, San Diego, CA, Aug. 2005, Paper 586711.
doi:10.1117/12.619133.

[29] Tappe, J. A., "Development of Star Tracker System for Accurate Estimation of Spacecraft Attitude," Ph.D. Thesis, Naval Postgraduate School Monterey, CA, 2009.

[30] Samaan, M. A., Steffes, S. R., and Theil, S., "Star Tracker Real-Time Hardware in the Loop Testing Using Optical Star Simulator," *Spaceflight Mechanics*, Vol. 140, AAS Paper 11-260, Springfield, VA, 2011, https://www.researchgate.net/profile/Malak_Samaan/publication/225025526_STAR_TRACKER_REAL-TIME_HARDWARE_IN_THE_LOOP_TESTING_USING_OPTICAL_STAR_SIMULATOR/links/56d9c65408aebabdb40f806b.pdf [retrieved 22 June 2018].

[31] Filipe, N., Jones-Wilson, L., Mohan, S., Lo, K., and Jones-Wilson, W., "Miniaturized Star Tracker Stimulator for Closed-Loop Testing of CubeSats," *Journal of Guidance, Control, and Dynamics*, Vol. 40, No. 12, Aug. 2017, pp. 3239–3246.

[32] Rössler, D., Pedersen, D. A. K., Benn, M., and Jørgensen, J. L., "Optical Stimulator for Vision-Based Sensors," *Advanced Optical Technologies*, Vol. 3, March 2014, pp. 199–207.
doi:10.1515/aot-2013-0045

[33] Bradski, G., "The Opencv Library," *Doctor Dobbs Journal*, Vol. 25, No. 11, 2000, pp. 120–126.

[34] Palo, S., Stafford, G., and Hoskins, A., "An Agile Multi-Use Nano Star Camera for Constellation Applications," *Conference on Small Satellites*, AIAA Paper SSC13-III-5, 2013.

[35] Woo, M., Neider, J., Davis, T., and Shreiner, D., *OpenGL Programming Guide: The Official Guide to Learning OpenGL, Version 1.2*, Addison-Wesley Longman Publishing Co., Inc., Boston, MA, 1999, pp. 247–260.

[36] Perryman, M. A., Lindegren, L., Kovalevsky, J., Hoeg, E., Bastian, U., Bernacca, P. L., Crézé, M., Donati, F., Grenon, M., Grewing, M., et al., "The HIPPARCOS Catalogue," *Astronomy and Astrophysics*, Vol. 323, No. 1, 1997, pp. 49–52.

[37] Giralo, V., and D'Amico, S., "Development of the Stanford GNSS Navigation Testbed for Distributed Space Systems," *Institute of Navigation, International Technical Meeting*, Inst. of Navigation, Reston, VA, 2018, pp. 837–856.

[38] Ardaens, J.-S., D'Amico, S., and Montenbruck, O., "Final Commissioning of the PRISMA GPS Navigation System," *22nd International Symposium on Space Flight Dynamics*, Vol. IV, Journal of Aerospace Engineering, Sciences and Applications, Oberpfaffenhofen, Germany, 2012, pp. 104–118.

[39] D'Amico, S., "Autonomous Formation Flying in Low Earth Orbit," Ph.D. Thesis, Technical Univ. of Delft, Delft, The Netherlands, 2010.

[40] Sharma, S., Beierle, C., and D'Amico, S., "Pose Estimation for Non-Cooperative Spacecraft Rendezvous Using Convolutional Neural Networks," IEEE Paper 978-1-5386-2014-4/18, New York, 2017, pp. 1–12. doi:10.1109/AERO.2018.8396425

[41] Sharma, S., Beierle, C., and D'Amico, S., "Towards Pose Determination for Non-Cooperative Spacecraft Using Convolutional Neural Networks," International Academy of Astronautics Paper IAA-ICSSA-17-01, 2017.

[42] Bowick, M., Cacciuto, A., Nelson, D. R., and Travesset, A., "Crystalline Order on a Sphere and the Generalized Thomson Problem," *Physical Review Letters*, Vol. 89, No. 18, 2002, Paper 185502. doi:10.1103/PhysRevLett.89.185502

[43] D'Amico, S., Benn, M., and Jørgensen, J. L., "Pose Estimation of an Uncooperative Spacecraft from Actual Space Imagery," *International Journal of Space Science and Engineering 5*, Vol. 2, No. 2, 2014, pp. 171–189. doi:10.1504/IJSPACESE.2014.060600

[44] Kremer, V. E., "Quaternions and SLERP," Univ. of Saarbrucken, Department for Computer Science, 2008, http://citeseerx.ist.psu.edu/viewdoc/download?doi=10.1.1.477.5820&rep=rep1&type=pdf [accessed 22 June 2018].

[45] Micchelli, C. A., "A Constructive Approach to Kergin Interpolation in R^k: Multivariate B-Splines and Lagrange Interpolation," *Rocky Mountain Journal of Mathematics*, Vol. 10, No. 3, 1980, pp. 485–497.

J. A. Christian
Associate Editor